

CHAPTER 7

ALL-OPTICAL PLASMONIC MODULATORS AND INTERCONNECTS

Domenico Pacifici, Henri J. Lezec, Luke A. Sweatlock, Chris de Ruiter, Vivian Ferry, and Harry A. Atwater

Thomas J. Watson Laboratories of Applied Physics, California Institute of Technology, 1200 E California Blvd., Pasadena, CA 91125, USA

We present experimental results and design guidelines for optical modulators and interconnects based on metallo-dielectric plasmonic structures. The short wavelengths and high field confinements of surface plasmon polaritons at the metal/dielectric interfaces allow for the manipulation and guidance of optical signals in very compact and power-efficient devices, amenable to ultra-large scale integration of on-chip optical functionalities.

1. Introduction

Relative to electrons, photons are characterized by lower heat dissipation, better immunity to crosstalk, lower dispersion, and huge information capacity due to their large bandwidths at optical frequencies. Because of these attractive features, researchers have long pursued the use of photons as the new information carriers, for demanding computations and optical data processing,^{1,2} and as a long-term solution to the interconnection bottleneck problem in microelectronics.³⁻⁵ Essential building blocks for all-optical computation and networks, such as logic elements and modulators, have already been demonstrated.⁶⁻⁹ However, despite the encouraging premises, all-optical integrated information processing has thus far remained elusive. Indeed, state-of-the-art optical modulators and interconnects typically rely upon weak, inefficient light-matter interactions, which call for large operating power

densities¹⁰ and long interaction distances (millimeters to centimeters),¹¹ thus limiting the opportunity for dense chip-based integration of all-optical functionalities. Moreover, due to diffraction, the wavelength of light typically sets a lower limit to further scaling down the feature size and increasing device density in conventional dielectric waveguide architectures.

Plasmonics, with its ability to confine and guide electromagnetic waves in subwavelength metallo-dielectric structures,^{12,13} promises to be a valuable alternative to the implementation of compact, fast and power-efficient optical integrated networks.¹⁴⁻¹⁶ In this chapter we investigate the use of subwavelength scatterers and corrugations in a metal as efficient, localized sources of surface plasmon polaritons (SPPs) propagating for several micrometers at the dielectric/metal interface. Several authors have reported, both theoretically and experimentally, that optical transmission through a subwavelength slit in metal films can be strongly influenced by the presence of nearby surface features, such as grooves or other slits.¹⁷⁻²⁴ We precisely measure and then modulate the propagation constants of the generated surface plasmon polaritons, using a set of surface wave interferometers consisting of a pair of parallel groove and slit, in which the distance between the slit and the groove is systematically varied up to several micrometers.²⁵

Light directly incident on the slit interferes with the propagating SPP, which originates from the groove and reaches the slit location with a phase shift determined by a characteristic scattering phase lag^{26,27} and a propagative phase depending on travelled distance. By varying the length of the interferometer arm, i.e. changing the distance between the slit and the groove, we determine the dispersion relation and propagation length of SPPs in a wide spectral range, i.e. from 400 to 1500 nm.

Active manipulation of the SPP is then achieved by coating the arm of the interferometer with an active medium, consisting, for instance, of a thin film of CdSe semiconductor quantum dots (QDs) fabricated by colloidal chemical synthesis in solution.²⁸ The QDs have been specifically designed to show an absorption bandgap at ~600 nm, therefore they can absorb high frequency surface plasmons (in the green-blue spectral range) while being transparent to surface plasmons at infrared wavelengths. Active modulation is achieved by means of two

co-propagating SPPs launched by the groove. A control (pump) SPP having a free-space wavelength of 514.5 nm is absorbed in photogeneration of electron-hole pairs inside the QD volume while propagating along the metal-dielectric interface. A signal (probe) SPP at 1.5 μm copropagating with the control SPP is then absorbed by promoting an intraband transition in the quantum dots, that is, by re-exciting the electron to a higher energy level. As soon as the pump SPP is turned off, the probe SPP is no longer absorbed, as the QDs quickly (in less than 40 ns) return to their transparent ground state. The modulated amplitude of the probe SPP determines a quick change in the interference conditions at the slit, thus causing a change in the interferometer output state (“on” and “off”). Thanks to the highly confined nature of the SPP field and the large quantum-dot absorption cross-section, the fast all-optical plasmonic modulation can be achieved at very-low power densities, in micrometer-scale planar devices.²⁵

We further design and fabricate a three-dimensional prototype of plasmonic modulator, employing a Mach-Zehnder interferometer in a multilevel metal-dielectric-metal stack, where the dielectric is made active by the presence of QDs. By opportunely varying the arms of the interferometers, higher modulation depths are achieved. Moreover, by exploiting the polarization properties of subwavelength slits in a metal film, we demonstrate optical isolation between the control and signal SPPs using cross-polarized incident beams incoupled into SPPs by perpendicularly-oriented slits. Finally, we present a design study for three-dimensional plasmonic vias and modulators, and investigate several schemes for coupling light into such devices, evaluating their power efficiency.

2. Surface plasmon interferometers

2.1. Fabrication and experimental methods

We fabricated several on-chip planar interferometers consisting of a single subwavelength aperture flanked by a subwavelength groove in a metal film. Identical subwavelength structures were fabricated by

focused ion beam (FIB) milling into a 400 nm thick layer of Ag evaporated onto flat fused silica microscope slides. A low beam current (50 pA) was used to achieve surface features defined with a lateral precision of the order of 10 nm and characterized by near-vertical sidewalls and a minimal amount of edge rounding. The milled groove and slit were 10 μm long, 200 and 100 nm wide, and 100 nm and 400 nm deep, respectively. The slit-groove separation distance was systematically varied in the range 500–10400 nm, in step of 50 nm, with a precision of 1%. A series of single apertures is also milled for reference purposes. The same set of structures was milled in another silver film (co-evaporated with the previous sample) which was previously spin-coated with a thin film of densely-packed CdSe QDs obtained by colloidal chemical synthesis in solution.²⁸ The QDs were capped with trioctylphosphine oxide (TOPO) ligands. Multiple spin-coatings of the toluene solution containing CdSe QDs were performed at 1000 rpm for 1 minute, followed by a thermal treatment at 150°C for 5 minutes. A 24 nm-thick film of densely-packed CdSe QDs was formed, with a good uniformity over the entire silver surface. The QDs showed bright photoluminescence (PL) peaked at 625 nm.

Transmission measurements were performed on both QD-coated and uncoated interferometers by focusing a laser beam onto the patterned side (Ag-air side) of each sample. The film thickness is such that the devices are optically opaque at the groove position, and light is only transmitted through the slit aperture. This approach allows us to achieve high signal-to-noise ratios in our experiments. The light intensity transmitted through the slit of each interferometer was gathered by a 50X microscope objective, sent to a single grating monochromator and detected with a liquid-nitrogen-cooled CCD array detector (spectral range: 400–900 nm), with an ultra-sensitive liquid-nitrogen-cooled germanium detector (spectral range: 900–1700 nm), or with a fast photomultiplier tube with an extended near-infrared spectral response (range 300–1700 nm).

Colour plate 1(a) at the end of the chapter displays a schematic of a typical interferometer consisting of a single slit of subwavelength width etched completely through a metallic film on a transparent substrate flanked by a single parallel groove, etched partially through the metal.

The center-to-center separation distance between slit and groove is defined as D . The blue spheres represent CdSe QDs. Two beams (signal and control) uniformly illuminate the structure. Diffractive scattering by the groove excites SPPs at two different frequencies, which we call the control and signal SPP, respectively. Colour plate 1(b) reports an SEM micrograph of an uncoated interferometer, with visible groove and slit.

2.2. Theoretical framework

Let us consider a TM-polarized (H field parallel to the longer slit side) electromagnetic plane wave with free space wavelength λ (and free space wavevector $k = 2\pi/\lambda$) impinging on the entire surface at an angle θ with respect to the sample normal. Diffractive scattering by the groove couples a fraction β of the incident field amplitude H into a surface wave with amplitude H_s that reaches the slit with an overall phase shift:

$$\varphi = kD \sin \theta + k_s D + \varphi_g + i \alpha D / 2, \quad (1)$$

where the first term is the phase shift due to the free-space optical path length difference between the incident wavefronts reaching the aperture and the groove, the second term is the phase shift gained by the surface wave traveling with surface wavevector $k_s = n_s k = 2\pi n_s / \lambda$ (where n_s is the real part of the effective refractive index of the surface wave), and the third term is the phase shift introduced by scattering at the groove. The fourth imaginary term in Eq. (1) accounts for absorption or scattering loss experienced by the surface wave propagating along the surface (where $\alpha = 4\pi\kappa/\lambda$ is the overall absorption coefficient, κ being the imaginary part of the effective refractive index of the surface wave). At the slit entrance, both the directly incident light and the SPP arriving from the groove are coupled into guided slit modes through diffractive scattering, with respective amplitude fractions γ and δ . The respective field amplitudes emerging from the slit are then given by $H_{T,s} = t\gamma H$ and $H_{T,g} = t\delta\beta e^{i\varphi}$, respectively, where t is the complex transmission coefficient of the slit. The two contributions can interfere if spatial and temporal coherence is maintained between them, in general when the coherence length of the optical beam is greater than the slit-groove distance. The total transmitted amplitude through the aperture is then

given by the following sum: $H_T = H_{T,s} + H_{T,g} = t(\gamma + \delta\beta e^{i\varphi})H$. Experimentally we observe the transmitted intensity:

$$I_T = |H_T|^2 = I_0 |1 + \eta e^{i\varphi}|^2, \quad (2)$$

where $I_0 = |t\gamma H|^2$ is the light intensity transmitted through an isolated slit (i.e. not flanked by a groove), and $\eta = \delta\beta/\gamma$ regroups the scattering efficiencies of the surface features. Eq. (2) can be written as:

$$T(P) \equiv \frac{I_T}{I_0} = 1 + \eta^2 e^{-\alpha(P)D} + 2\eta e^{-\frac{\alpha(P)D}{2}} \cos[kD(\sin\theta + n_s) + \varphi_g] \quad (3)$$

where $\alpha(P)$ is the absorption coefficient which we intend to modify with an external control beam of power P . Eq. (3) shows that maxima and minima in transmitted light intensity as a function of slit-groove distance result from constructive or destructive interference between the surface wave launched by the groove and the incident wave at the slit position.

There are several terms in Eq. (3) suggesting that such a slit-groove surface-wave interferometer could constitute an efficient all-optical modulator. Indeed, under the particular condition $kD \gg 1$, a small change in the real part of the refractive index n_s could produce a surface-wave phase shift of sufficiently high magnitude (relative to the fixed phase of the light directly illuminating the slit) to change a transmission maximum into a minimum or vice-versa, thus enabling the possibility of phase-modulating a probe signal. In another approach, for sufficiently long slit-groove distances D , a small change in the absorption coefficient α could lead to substantial attenuation of the surface wave during its trip from the groove to the slit. This would suppress interference with the light directly illuminating the slit, thus producing amplitude-modulation of the transmitted light. It is this second approach which we explore in the following sections.

2.3. Uncoated plasmonic interferometers

First we characterize the optical properties of uncoated interferometers. The top panel of Fig. 1 shows a schematic of the experiment; a single interferometric device is uniformly illuminated by an optical Gaussian beam. Diffractive scattering by the groove excites an SPP which propagates along the metal/air interface and interferes with the incident

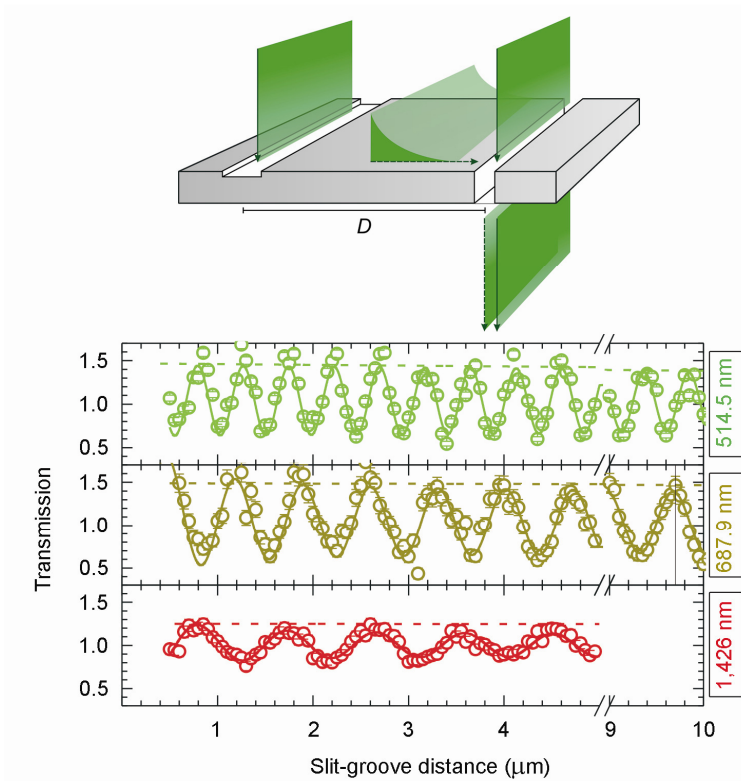


Fig. 1. Top panel: schematic of an uncoated interferometer consisting of a slit and a groove, uniformly illuminated by an optical beam normally incident on the metal surface. Bottom panels: measurements of the light intensity transmitted through the slit of a series of uncoated interferometers with different arm length (slit-groove distance), at various wavelengths.

beam at the slit position. Light transmitted through the slit carries information of the interference process between the reference beam (directly incident on the slit) and the propagating surface wave. The bottom panels of Fig. 1 report measurements of the light intensity transmitted through a set of interferometers with different arm lengths, i.e. slit-groove distance D , at various laser wavelengths ($\lambda=514.5$ nm, 687.9 nm, and 1426 nm, respectively). The angle of incidence is 0° in the first two cases and 32° in the third. The total power density incident on the sample surface is fixed at ~ 0.5 W/cm² in all three cases. The intensity

of light transmitted by an isolated reference slit is used to normalize the transmission data through each device.

Compiling the normalized data yields a plot of normalized transmitted intensity as a function of slit-groove distance (where each open circle corresponds to a device with a specific slit-groove distance). Several features are apparent in Fig. 1: (1) at a given incident free-space wavelength λ , the normalized transmission through the subwavelength slit shows oscillatory behavior as a function of the slit-groove distance, as a result of constructive or destructive interference between the incident beam and the surface wave launched by the neighboring groove, (2) the spatial period of this oscillation increases with increasing λ , and (3) the envelope of the oscillation amplitude remains approximately constant as a function of interferometer arm length, suggesting that within the investigated spectral range, surface waves can propagate for several micrometers without significant loss.

The observed enhancement and suppression of the intensity transmitted through the slit can be explained within the theoretical framework developed in section 2.2. Using Eq. 3 with $k = 2\pi/\lambda$, D , and θ as known parameters, fits are performed to the data reported in Fig. 1, and shown as solid lines. These fits yield important physical parameters such as the surface wave launching efficiency η , which is about 20-25% in the investigated spectral range, the phase lag caused by diffraction at the slit φ_g , which depends on groove depth and it is approximately $\pi/2$, the absorption coefficient α and the effective refractive index n_s . In Fig. 2 we plot the derived value of the effective surface wave index n_s as a function of free-space wavelength λ (solid symbols) and compare it (continuous line) to the effective refractive index expected for an SPP at an Ag/air interface:¹³

$$n_{SPP} = \text{Re} \left[\left(\frac{\varepsilon_1 \varepsilon_2}{\varepsilon_1 + \varepsilon_2} \right)^{1/2} \right], \quad (4)$$

where ε_1 is the complex dielectric constant of Ag, experimentally determined by ellipsometry, and $\varepsilon_2 = 1$ is the dielectric constant of air. The excellent agreement between the experimental data reported in Fig. 2 as solid symbols and Eq. (4), within the experimental errors, suggests

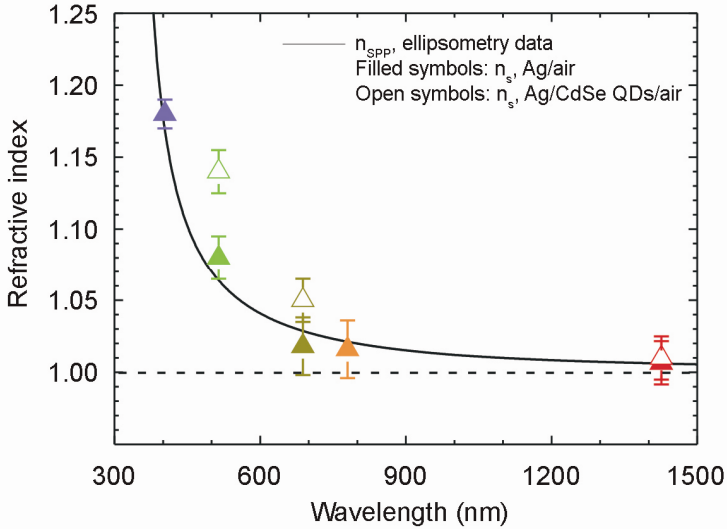


Fig. 2. Refractive index of the propagating surface wave modes as extracted by transmission measurements through uncoated and QD-coated interferometers.

that the long-range propagating surface wave is indeed an SPP. This demonstrates that diffractive scattering from a single subwavelength groove in a metal film can be an efficient source of guided surface plasmons at a metal-dielectric interface, indeed more compact than bulky prism- or grating-coupling approaches.

2.4. QD-coated plasmonic interferometers

In order to actively modify the propagation constants of the SPP launched by the groove, we coated the metal with a thin layer of semiconductor quantum dots, as explained in the previous experimental section.

As shown in Fig. 3, when excited by a laser beam at 404 nm the CdSe QDs show bright PL peaked at 625 nm with a FWHM of 32 nm, and red-shifted with respect to the 1S absorption edge which occurs at 595 nm, as evidenced by the absorption curve reported in Fig. 3. This emissive state is generally attributed to splitting of the lowest hole state as a result of crystal field and e-h exchange interaction,^{29,30} as shown in the right inset

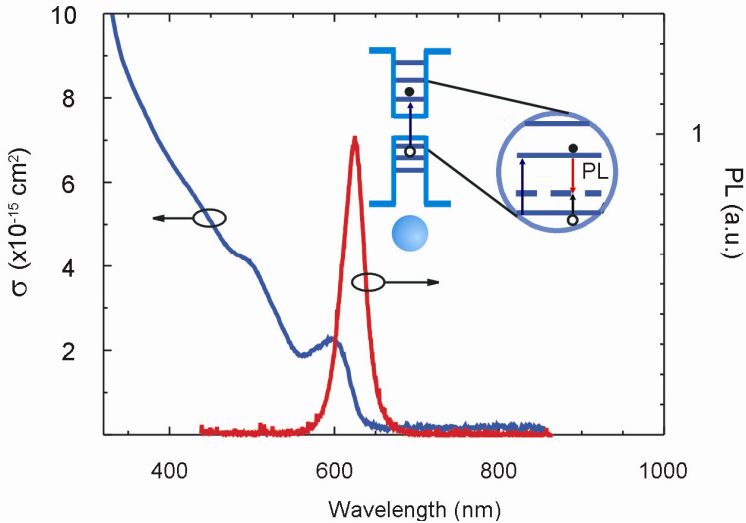


Fig. 3. Absorption cross section (σ) and photoluminescence spectrum (PL) for CdSe QDs. Insets: energy level scheme for a QD.

to Fig. 3. Both the PL and the absorption of the CdSe QD ensemble show broad features, indicating both homogeneous and inhomogeneous level broadening caused by the crystal-field induced removal of level degeneracy and by the size distribution of nanocrystals, respectively. It is interesting to note that the CdSe QDs have relatively high absorption cross section in the visible.³¹ For example the measured absorption cross section at 514.5 nm is $3.5 \times 10^{-15} \text{ cm}^2$. This value is 6 orders of magnitude higher than the typical absorption cross sections for atomic-like transitions in rare-earth ions, which are extensively used in telecommunication and as promising active materials in microphotonics.³² To understand the role of the thin layer of CdSe QDs, we performed transmission experiments on similar slit-groove interferometers coated with QDs, and with varying arm distances. A schematic of the transmission experiment is reported in the top panel of Fig. 4. The normalized light intensities transmitted through the slit of various interferometers are reported in the bottom panels of Fig. 4, as a function of slit-groove separation distance, and at various free-space wavelengths λ . The first interesting observation is that the transmission maxima and minima occur at shorter slit-groove distances. This effect is

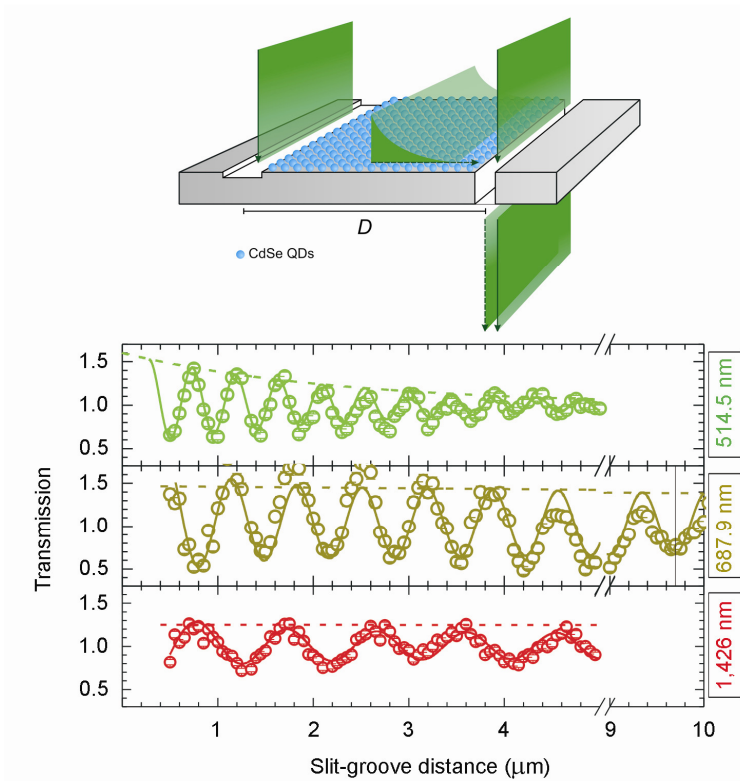


Fig. 4. Top panel: schematic of a QD-coated interferometer uniformly illuminated by an optical beam at normal incidence. Bottom panels: measurements of the light intensity transmitted through the slit of a series of QD-coated interferometers with different arm lengths (slit-groove distance), at various wavelengths.

particularly evident in interferometers with long arms. For example, the normalized light transmission through an interferometer with $D=9.7 \mu\text{m}$ (indicated by vertical lines in Fig. 1 and Fig. 4, $\lambda=687.9 \text{ nm}$) goes from a maximum (constructive interference) without QD-coating (Fig. 1) to a minimum (destructive interference) in the presence of QDs (Fig. 4). Such a remarkable change in the interference conditions can be achieved by a slight variation in the effective refractive index. Indeed, using Eq. (3) it is possible to fit the data in Fig. 4, and estimate the effective refractive index experienced by the surface wave n_s while propagating at the QD-coated metal interface. The fit values are reported in Fig. 2 as open

symbols. The SPP refractive index systematically increases relative to the case of the uncoated interferometers, due to the presence of the high-refractive index film of CdSe QDs. The increase is consistent with calculations of the SPP mode profile and modal overlap with the CdSe QD layer, whose refractive index was measured by spectroscopic ellipsometry as a function of wavelength. We note that at $\lambda=1426$ nm the value of n_s is only marginally higher in the case of the coated sample compared to that of the uncoated sample. At $\lambda = 514.5$ nm, n_s is 6% higher in the QD-coated interferometer, consistent with an increased mode overlap with the QD layer due to the smaller skin depth of the SPP at shorter wavelengths.

Another striking result arises from a close comparison between the transmission data at $\lambda=514.5$ nm in Fig. 4 and Fig. 1, that is the envelope of the oscillating normalized transmission strongly decreases with slit-groove distance in the presence of QDs (Fig. 4, $\lambda=514.5$ nm), while it is approximately constant for the uncoated sample (Fig. 1, $\lambda=514.5$ nm). The extracted absorption coefficient α increases from 400 cm^{-1} without the QD layer to 8200 cm^{-1} with the QD layer. At first one may be tempted to explain the increased absorption by out-of-plane scattering of the SPP by the QDs. This hypothesis is easily ruled out by looking at the transmission data at longer wavelengths. Since Rayleigh scattering depends on the fourth power of the incident wavelength, one would expect stronger absorption at longer wavelengths. However, the oscillating transmission data at $\lambda=687.9$ nm and $\lambda=1426$ nm in Fig. 4 show a constant envelope amplitude as a function of slit-groove distance, similar to the uncoated case, suggesting that no substantial absorption is indeed occurring.

Instead, the increased absorption can be explained in terms of plasmonic excitation of electron-hole pairs in the QDs. For a nanocrystal radius of 2.4 nm, and a close-packed distribution of QDs, the estimated QD concentration in the film is $\rho \sim 1 \times 10^{19} \text{ cm}^{-3}$. We estimate an SPP mode overlap with the 24-nm thick CdSe film $\Gamma \sim 25\%$. Therefore, the calculated effective absorption coefficient at $\lambda=514.5$ nm would be $\alpha = \Gamma \sigma \rho = 8750 \text{ cm}^{-1}$. This value is in very good agreement with the value (8200 cm^{-1}) extracted from the fitting procedure, and strongly support the hypothesis that the QDs are indeed absorbing the propagating

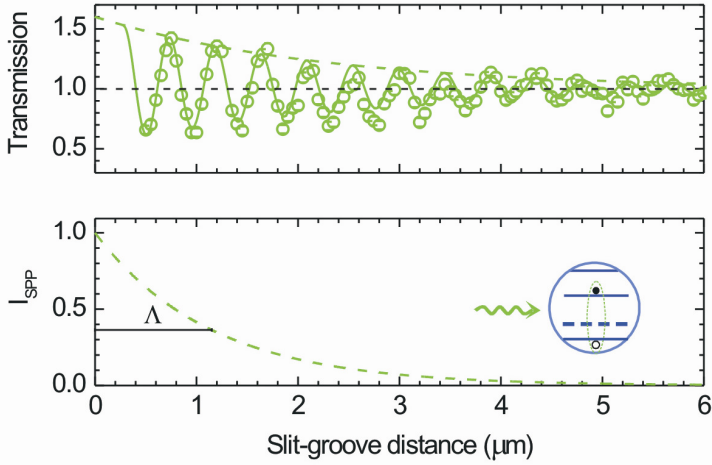


Fig. 5. Interferometry at $\lambda=514.5$ nm for QD-coated devices. Top panel: transmission measurements for a series of QD-coated interferometers with different arm length (slit-groove distance). Bottom panel: SPP intensity at the slit position as a function of slit-groove distance.

SPP at $\lambda=514.5$ nm. To stress this point, in Fig. 5 we report the transmission data at $\lambda=514.5$ nm for the QD-coated sample (top panel) together with the extrapolated values of the SPP intensity measured at the slit position (bottom panel), as a function of slit-groove distance. The SPP intensity decreases exponentially with an experimental decay constant (propagation length) $\Lambda = 1.2 \mu\text{m}$, again in good agreement with the value estimated by assuming bandgap absorption in the QDs (which gives $\alpha^{-1} = 1.14 \mu\text{m}$). The emerging picture is therefore the following: (1) SPPs with energy above the QD bandgap can be absorbed by CdSe QDs while propagating along the metal/dielectric interface, with subsequent photogeneration of bound electron-hole pairs (excitons) in the QD volume, as shown in the schematic of Fig. 5; (2) for sufficiently long interferometers, the SPP generated at the groove location can be completely absorbed by the QDs, and is no longer able to reach the slit; therefore, neither constructive nor destructive interference between the SPP and the incident beam at the slit position can occur, and the normalized transmission intensity tends to 1 (Fig. 4, $\lambda=514.5$ nm); (3) SPPs having energy smaller than the QD bandgap cannot be absorbed by

the nanocrystals, thus they can propagate without attenuation, reach the slit and interfere with the incident beam, causing either constructive or destructive interference at the slit output mouth.

2.5. All-optical modulation in QD-coated plasmonic interferometers

So far we have studied the optical properties of plasmonic interferometers illuminated by a single light beam at a time. In all-optical modulators, two different light beams are generally employed: one of the two beams (control) is used to copy information onto the other (signal) at a different wavelength. In order to achieve modulation, the two beams, which are otherwise independent, need to be coupled by using some nonlinearity of the medium in which they propagate. Our intent is to use a control beam in the form of a propagating SPP to change the absorption coefficient α for another co-propagating signal SPP at a different frequency. The signal SPP interferes with the incident field at the slit, and the total light intensity transmitted through the slit is given by Eq. (3).

The exponential function of α provides for the necessary non-linear interaction between the two co-propagating SPPs. We performed continuous-wave pump ($\lambda=514.5$ nm, $\theta=0^\circ$) and probe ($\lambda=1426$ nm, $\theta=32^\circ$) transmission measurements on various quantum-dot coated interferometers. As illustrated in the schematic diagram of Colour plate 1(a), the control and signal beams simultaneously and uniformly impinge on the sample surface and are scattered by the subwavelength groove which launches two co-propagating SPPs with different energies (represented in green and red, respectively) towards the slit. The SPP at $\lambda=514.5$ nm is strongly absorbed by the CdSe QDs, while the SPP at $\lambda=1426$ nm propagates without absorption in the absence of the pump SPP. First we consider a structure with a slit-groove distance $D=3.6$ μm which displays a relative maximum in normalized transmission intensity at $\lambda=1426$ nm in absence of pump illumination (Fig. 4, $\lambda=1426$ nm). The top panel of Colour plate 2 displays (open symbols) the normalized transmission intensity of this device at $\lambda=1426$ nm as a function of the pump power at $\lambda=514.5$ nm. Both probe and pump beams are chosen to have TM polarization (H-field parallel to the slit and groove long axis).

The normalized transmitted probe intensity decreases as a function of pump power, reaching a minimum at a power density of $\sim 600 \text{ W/cm}^2$, and then slightly increases as the pump power is increased further. Since the transmission enhancement for that particular device at zero pump power results from constructive interference between the SPP and the incident beam at the slit position, a decreased transmission can only be explained by attenuation of the surface wave due to an absorption process that is activated by the pump beam.

We propose that it is confined carrier absorption from excited CdSe QDs which attenuates the probe surface wave at $\lambda=1426\text{nm}$. In this model (schematic shown in the left inset of Colour plate 2) a confined exciton is first generated in a CdSe QD by photo-absorption of a control SPP at $\lambda=514.5\text{nm}$. The signal SPP at $\lambda=1426 \text{ nm}$ then re-excites the exciton by bringing the electron into a higher lying energy level of the QD, and is therefore absorbed. By increasing the pump power, a larger fraction of QDs is excited, and as a consequence more probe SPPs are absorbed. This phenomenon is analog to the free carrier absorption (FCA) of photons propagating in bulk semiconductors where free carriers are generated by thermal ionization of the dopants or by optical excitation of electron-hole pairs. The dynamics of this mechanism have been extensively studied in thick films of CdSe QDs by femtosecond transient absorption spectroscopy in the visible and near-infrared spectral ranges.^{33,34}

If we denote with σ_{CCA} the cross section for the confined carrier absorption of a propagating signal SPP by an excited QD, the photoinduced absorption coefficient is then equal to:

$$\alpha = \Gamma_s \sigma_{CCA} \rho^* \quad (5)$$

with Γ_s the mode overlap of the signal SPP with the active layer, and ρ^* the density of excited quantum dots in steady state. Approximating the QD with a two-level system, ρ^* is given by the following equation:

$$\rho^* = \frac{\sigma \phi \tau}{\sigma \phi \tau + 1} \rho, \quad (6)$$

where ρ is the total concentration of QDs in the film, ϕ is the fraction of control SPP flux parallel to the metal/dielectric interface overlapping with the active film (in $\text{cm}^{-2} \text{ s}^{-1}$), σ the QD absorption cross section at the

pump wavelength, and τ the recombination lifetime of an excited QD. In the low pump power regime, such that $\sigma\phi\tau \ll 1$, Eq. (6) becomes:

$$\rho^* = \sigma\phi\tau\rho, \quad (7)$$

where ϕ can be calculated using the Poynting theorem and integrating the magnitude of the Poynting vector over the active region. Without loss of generality, ϕ is a linear function of the incident pump power density P :

$$\phi = \eta_c \frac{P}{\epsilon}, \quad (8)$$

with η_c an effective coefficient taking into account the incoupling efficiency, scattering cross section of the groove, and mode overlap of the control SPP with the active layer, and $\epsilon = h\nu$ the energy of an SPP of frequency $\nu = c/\lambda$, with h and c the Planck's constant and speed of light, respectively.

By combining the previous equations, Eq. (5) becomes:

$$\alpha(P) = \eta_c \Gamma_s \sigma_{CCA} \sigma \tau \rho \frac{\lambda}{hc} P, \quad (9)$$

which proves that $\alpha(P)$ is a linear function of the incident pump power density P .

To demonstrate that the observed all-optical modulation of light intensity at $\lambda=1426$ nm transmitted through the slit results solely from excitation of the CdSe QDs by the control SPP at $\lambda=514.5$ nm and not from direct illumination of the QDs by the incident pump beam, we changed the polarization of the pump beam at $\lambda=514.5$ nm from TM to TE (electric field parallel to the slit and groove long axis), a polarization for which no surface wave can be launched by the groove or the slit. When the two-colour pump-probe experiment is repeated under these conditions as a function of pump power (Colour plate 2, solid symbols), no significant modulation of transmitted intensity is observed as a function of pump power.

The lack of transmission modulation in absence of the surface wave shows that direct illumination of the surface is a negligible source of QD excitation over the explored range of pump powers. This is not surprising since the sum of the incident and reflected fields has, at normal incidence, a node at the metal-air interface, leading to a negligible contribution to optical power density in the CdSe-QD layer. On the other hand, the field amplitude of the control SPP launched by the groove has a

maximum right at the interface, guaranteeing maximum mode overlap with the active QD layer. We conclude that the large amplitude transmission modulation observed in the case of a TM-polarized pump beam is the direct result of excitation of the CdSe QDs by a surface wave at that frequency launched by the groove and the slit.

For an interferometer with aperture-groove distance $D=2.15 \mu\text{m}$ a transmission minimum occurs at $\lambda=1426 \text{ nm}$, as shown in Fig. 4. The probe transmission variation with pump power through this particular device is given in the bottom panel of Colour plate 2. Unlike the variation observed for a distance corresponding to a transmission maximum, the intensity increases as a function of pump power density and then starts to decrease again with increasing pump power. In this case, photoinduced absorption of the probe SPP reduces its destructive interference with the incident beam at the slit, and thus increases the overall normalized transmission, making it closer to that of an isolated slit, i.e. equal to 1.

Figure 6 illustrates the temporal response of the transmitted signal to the pump excitation, for a $3.6\text{-}\mu\text{m}$ -long interferometer. At $t=0 \mu\text{s}$ the pump beam, modulated at a frequency of 250 Hz, is turned on at a power density of 500 W/cm^2 , and the probe transmission intensity shows an abrupt decrease. The switching time of the device is below the temporal resolution of our experimental set up ($\sim 40 \text{ ns}$). In order to better establish the timescale for the modulation effect, the frequency response of the probe signal to pump modulation was measured (Fig. 6, inset) from 1 to 1,000 Hz using a mechanical chopper, a Ge detector and a lock-in amplifier (solid triangles), and from 250 Hz to 50 MHz using an acousto-optic modulator, a photomultiplier-tube (PMT) detector extended in the near infrared and a multichannel scaler (solid circles). The change in probe signal (modulation depth) as a function of pump modulation frequency is constant up to 25 MHz, which again establishes a timescale of $\sim 40 \text{ ns}$ for the modulation effect (the roll-off at the end of the explored frequency range corresponding to the response time of our measurement system). The inferred response time of the device at $\sim 40 \text{ ns}$ is consistent with our suggested mechanism for device operation, consisting of probe SPP absorption by a fast intraband transition in the

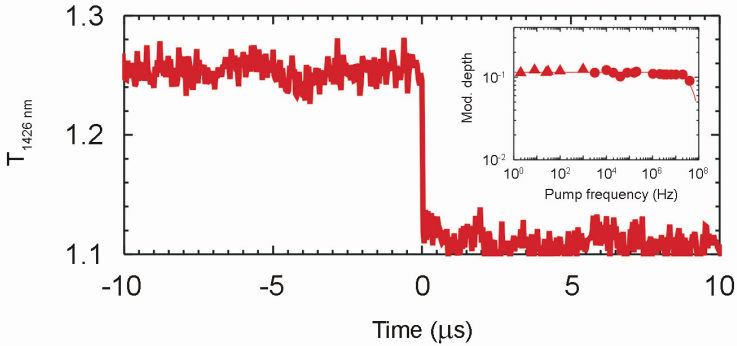


Fig. 6. Variation of the probe intensity transmitted through the slit of a 3.6- μm -long interferometer as a function of time; at $t=0$ μs the pump beam is turned on, and a fast (<40 ns) decrease in probe transmitted intensity is observed, due to photoinduced absorption in excited QDs. Inset: variation of the probe signal as a function of pump beam modulation frequency, at a power level of 500 W/cm^2 .

CdSe QDs excited by the control SPP. The data reported in Fig. 6 clearly demonstrate the possibility of achieving modulation frequencies that are orders of magnitude faster than typical frequency responses of modulators relying on thermal effects, which are typically in the range of a few Hz. At power densities >600 W cm^2 , both interferometers shown in Colour plate 2 experience a recovery of their original (that is, zero-pump) transmission values, owing to a reduction in absorption of the probe SPP from excited QDs.

In Fig. 7(a), the transmission intensity at $\lambda=514.5$ nm for QD-coated interferometer with a 2.6 μm slit–groove distance is shown to increase as a nonlinear function of pump power (open symbols). The transmission is at first equal to that of an isolated slit, due to QD-absorption of the SPP. At high pump powers, the transmission reaches values typical for an uncoated device (compare with Fig. 7(b), open symbols), in which no absorption from the QD occurs. The decrease in probe-SPP attenuation at high pump excitation rates is due to a two-photon process in which a pump SPP is absorbed by a previously excited QD, producing an electronic photo-ionization event that leads to charge trapping at nearby surface states. The QD is thereafter transparent to either incoming pump or probe SPPs (schematic inset of Fig. 7(a)).

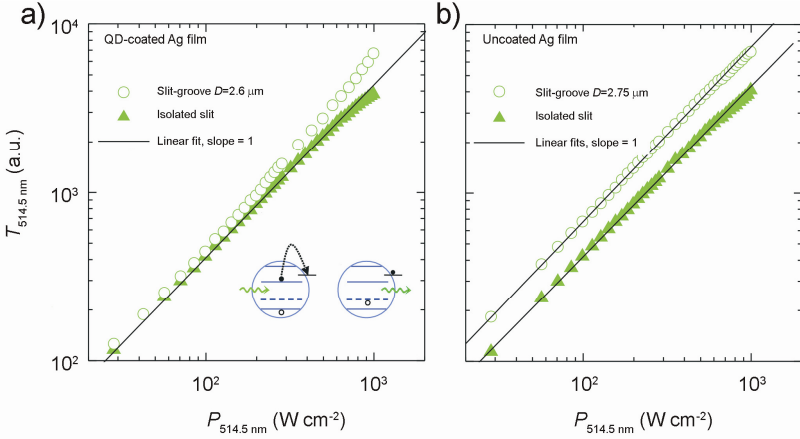


Fig. 7. Power dependence of the pump beam transmission at $\lambda=514.5$ nm. (a) Light intensity at $\lambda=514.5$ nm transmitted through the slit of a QD-coated interferometer with slit-groove distance $D=2.6$ μm (open symbols), and through an isolated slit (solid symbols); inset: schematic diagram of photoinduced bleaching in a QD. (b) Transmitted intensity at $\lambda=514.5$ nm as a function of power for an uncoated sample.

On the other hand, Fig. 7(b) indicates that pump transmission through an uncoated interferometer is instead linear at all powers, further confirming that the modulation effect observed in the QD-coated sample is not due to thermal or non-linear effects in the metal film, but to plasmon-induced absorption in CdSe QDs.

We note that a pump power density of ~ 100 Wcm^{-2} impinges on a groove area of 2×10^{-8} cm^2 , so the total power incident on the groove is 2 mW. The experimentally determined power incoupling efficiency into an SPP is $\sim 10\%$, so the pump SPP power is ~ 200 nW, or ~ 20 $\text{nW } \mu\text{m}^{-1}$ per groove length. Thus, a 1- μm -long groove would enable modulator power operation at only 20 nW. In our scheme, based on fast intraband electronic transitions in QDs, the modulation switching time is ultimately limited by the QD exciton recombination lifetime (≤ 40 ns in our system), yielding an estimated minimum switching energy per operation of approximately 800 aJ. These results suggest the potential of our approach for chip-based all-optical modulator arrays whose switching energies may rival those of fully scaled Si-based CMOS electronic inverters.

3. Three-dimensional plasmonic modulators

3.1. New designs for improved figures of merit

In 2005, the ITRS set the requirements for a basic all-optical switching element, namely: it should (1) work at around 1.5 μm , (2) operate at low power, and (3) have a small component size. The planar interferometers presented so far are interesting because they fulfill all of these requirements. Nevertheless, the proof-of-concept design is affected by some important drawbacks that we would like to address and overcome.

First of all, even though the planar interferometers are characterized by a fast switching time and high modulation frequency, the typical modulation depth is relatively small, of the order of only $\sim 10\text{-}20\%$. This is determined by the fact that even though the signal SPP is completely extinguished by photoinduced absorption in excited QDs, the light transmitted through the slit can never be zero, since the slit is always illuminated by the incident beam. A way to overcome this problem maintaining the same geometry would be to use localized excitation sources, such as the subwavelength aperture of a near-field optical microscope, to illuminate the groove and not the slit. In such a way, when the probe beam is on, the transmission through the slit is determined only by the propagating SPP term, i.e. $H_T = H_{T,g} = t(\delta\beta e^{i\varphi})H$, since the slit contribution is now $H_{T,s} = 0$. The normalized transmission in this case would be:

$$T(P) \equiv \frac{I_T(P)}{I_T(P=0)} = \frac{|H_T(P)|^2}{|H_T(P=0)|^2} = e^{-\alpha(P)D}, \quad (10)$$

where we have explicitly considered the power dependence of the absorption coefficient. In the absence of pump power, that is $P = 0$, $\alpha(P)D \ll 1$ and the normalized transmission through the slit is equal to "1," corresponding to the "on" state of the device. As soon as the pump beam is turned on, and the power set such that $\alpha(P)D \gg 1$, the signal SPP is completely absorbed by the excited QDs. Therefore no signal SPP can reach the slit, which in turn reduces the transmitted intensity to zero. Such a strategy would certainly enable orders of magnitude increase in modulation depth. However, this approach is not easy to implement in integrated dense optical chips.

Therefore, in order to solve the problem in a way that may lead to more realistic architectures, we designed and fabricated a novel plasmonic modulator, whose schematic and principle of operation are reported in Colour plate 3. The interferometer consists of a metal/dielectric/metal waveguide, and makes use of two slits milled in the top metal layer to incouple the incident beam into SPPs propagating in the dielectric waveguide. The dielectric can be a semiconductor, or even an insulating matrix codoped with CdSe quantum dots. By opportunely choosing its thickness, the dielectric layer can be made to only support the fundamental plasmonic mode while cutting-off all of the higher order photonic modes. A slit in the bottom metal layer collects the propagating SPPs; the interfered field is then guided in the slot cavity provided by the slit and scattered back in free space, at the bottom side of the device. It is interesting to note that this design could be merged with modern microelectronic circuits, by simply placing a CMOS-based detector right at the bottom output of the out-coupling slit. The device depicted in Colour plate 3 resembles a miniaturized Mach-Zehnder interferometer, with arms A and B, having lengths D_A and D_B , respectively. When the two input slits are coherently and uniformly illuminated with a signal beam at normal incidence, SPPs with field amplitudes $H_{SPP,A}$ and $H_{SPP,B}$ are launched and guided into the dielectric waveguide with the same amplitude βH and the same incoupling phase lag φ_0 (analogous to φ_g in Eq.(1)); the SPPs propagate with wavevector $k_{SPP} = n_{SPP}k$ and reach the outcoupler slit with a relative phase shift:

$$\Delta\varphi = \varphi_A - \varphi_B = \left(k_{SPP} + i \frac{\alpha(P)}{2} \right) (D_A - D_B), \quad (11)$$

which determines the interference condition between the two SPPs at the output slit position. For interferometers with relatively small arms, the material loss in the absence of pump power is negligible, and we can safely assume $\alpha(P = 0) = 0$ in Eq. (11). The same arguments holds true if we choose the difference in optical path such that $\alpha(P = 0)(D_A - D_B) \ll 1$. Either way, in the absence of a pump beam, by setting the distance of the two arms of the interferometer in such a way that the two SPPs are exactly out of phase, that is $\Delta\varphi = \pi$, the two SPPs perfectly cancel out at the slit position, thus determining an exact null in transmitted intensity through the bottom slit; this is the “off” state of the modulator. The condition for destructive interference can be altered by

affecting the propagation of the SPP in one of the two arms using a pump SPP. For example, we could excite a control SPP in one of the two arms, say arm B, which would induce free-carrier absorption of the signal SPP propagating in arm B. This in turn would prevent the destructive interference with the other signal SPP propagating in arm A, which would then be transmitted through the slit, determining the “on” state of the modulator.

Another drawback of the simple planar proof-of-concept approach previously investigated in section 2 is that the control and signal SPPs are excited using the same subwavelength object (a groove), co-propagate in the modulator and are simultaneously transmitted through the slit. For many applications it would be desirable to maintain optical isolation between the two beams. Typically, this can be accomplished by using a filter in the far field to selectively transmit the frequency of interest. This approach is of course not convenient for large scale integration of the device. Therefore we recur to another trick. Subwavelength slits are very good polarizers, in that they can only transmit light with H-field component parallel to their long-axis (TM-polarized beam). At the same time, the launching efficiency for long-range propagating SPPs is maximum when the slit is illuminated with TM-polarized beams, and it goes to zero for TE-polarized beams. Therefore, to achieve the desired isolation, we use cross-polarized signal and control beams, and slits that are perpendicular to each other to independently incouple signal and control SPPs, respectively.

A practical implementation of the Mach-Zehnder plasmonic interferometer consists of two thermally evaporated 300-nm-thick silver films separated by a core layer of SiO₂ codoped with chemically synthesized CdSe colloidal quantum dots (QDs), capped with a different ligand (tris-hydroxypropylphosphine, THPP) to make them soluble in the spin-on-glass matrix. The size of these QDs is engineered such that in the ground state the QDs are transparent to the probe light, but once an exciton is created, the QDs can absorb the probe. Several devices have been fabricated by sequential evaporation of metal films, spin-coating of spin-on-glass codoped with QDs, and focused ion beam milling. Parallel slits are milled in the top and bottom silver films and aligned to previously milled slits in the bottom metal layer. To selectively create

excitons only in one arm, slits parallel to the interferometer arm B are milled by FIB on the top metal layer. Pump light cross-polarized with respect to the probe beam is selectively coupled into this arm only.

An SEM micrograph of an array of 9 plasmonic Mach-Zehnder interferometers is shown in Colour plate 4(a). In this array, the length of arm A is varied from 2 μm (bottom device) to 2.4 μm (top device). A cross section of one of the devices is shown in Colour plate 4(b). Smooth core-cladding interfaces are clearly present, preventing SPPs from scattering loss in the waveguide. Colour plates 4(b) and (c) show, superimposed to the SEM micrographs, the working principle of the proposed modulator. In Colour plate 4(b) the device is uniformly illuminated with a probe beam, TM polarized, that is with magnetic field oscillating parallel to the long axis of the incoupling slits. Since the top metal layer is optically thick, light can only be transmitted through the two slits which act as the mirrors of the interferometer. Light transmitted through each slit is then coupled into SPPs propagating to the left and right of each slit.

We focus our attention on the SPPs that propagate toward the output slit milled in the bottom metal layer. By opportunely choosing the length of the two interferometric arms (designated with A and B in Colour plate 3) a destructive interference can be set such that the light intensity transmitted through the outcoupling slit is zero, or a minimum value. This scenario represents the “off” state of the modulator, which would correspond to a logic state “0.” In Colour plate 4(c) the device is also illuminated with a pump beam which is cross-polarized with respect to the probe signal. Light can leak through the vertically aligned slits which act as sources of SPPs which propagate in the direction perpendicular to the right arm of the interferometer (arm B in Colour plate 3). These SPPs act as control beams in that they excite the QDs present in the dielectric and determine a photo-induced absorption of the probe SPP, as explained in section 2 for planar plasmonic interferometers. The signal SPP propagating in the right arm of the interferometer is absorbed along its path by free-carrier absorption in the excited QDs and is no longer able to reach the output slit. Therefore the destructive interference with the SPP propagating in the left arm is no longer possible. Light can now emerge through the slit, and the state of the modulator is set to “on,”

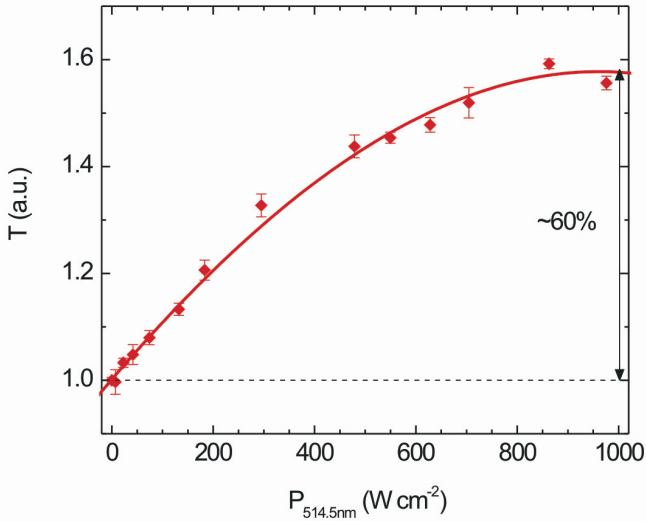


Fig. 8. Pump-power dependence of the transmitted probe intensity at 687.9 nm through a plasmonic modulator that shows a minimum in probe transmission at zero pump power. The solid line is a guide to the eye.

(logic state “1”). It is important to stress that the control SPPs are characterized by a longitudinal electric field oscillating in the direction parallel to the long axis of the output slit. For this polarization, no transmission of the pump beam is observed through the slit, which guarantees optical isolation between the control and the signal beams.

We experimentally investigate the operation of such interferometers by performing pump and probe experiments. First, the probe transmission through the Mach-Zehnder plasmonic interferometers is studied as a function of the length of interferometer arm A. In practice, we scan the length of one of the two interferometer arms (arm A in this case) and look for a device that shows a minimum in transmission. When this condition is satisfied, destructive interference between the two SPPs is taking place at the slit. We find that a destructive interference state is obtained for a device with an interferometer arm length $D_A = 2.55\mu\text{m}$. Results of pump-probe experiments for such a device are presented in Fig. 8. Simultaneous illumination with both pump and probe light beams results in an increase of the transmitted probe intensity. By varying the

power density, the probe signal transmission at 687.9 nm increases up to 60% with respect to the zero-pump value, as the result of increased absorption of the signal SPP propagating in the right arm of the interferometer.

4. Design of plasmonic modulators and interconnects

Inspired by the previous experimental results, we employ finite-difference time domain (FDTD) simulations to evaluate the performance of higher complexity plasmonic waveguide structures which are not readily tractable by analytic methods.

4.1. Multilevel plasmonic modulators and interconnects

In the following section, we study a multilayer metal/dielectric stack which defines two horizontal dielectric waveguides, separated from each other by a 150-nm-thick layer of Ag cladding. The cladding metal layer is thick enough to be optically opaque, thus suppressing crosstalk due to mode coupling between the top and bottom waveguides. Slits milled in the central metal cladding play the role of optical “vias” between the two dielectric waveguides. A subwavelength slit in the top metal layer acts as optical incoupler in the first waveguide, and three slits milled in the bottom metal layer serve as optical outcouplers. All the slits are 50 nm wide. A schematic cross section of the structure is reported in Fig. 9(a). When illuminated by an optical beam, the slit in the top metal layer is found to be effective at scattering light into guided modes of the first buried metal/dielectric/metal waveguide. These guided modes are launched with propagation direction transverse to the slit long axis. Two slits in the central metal layer partially scatter the guided modes into guided modes of the underlying waveguide. The waveguide dielectric cores are here modeled as a purely transparent dielectric with $n = (2.02+0i)$, corresponding to that of QD-doped silicon dioxide at the excitation wavelength $\lambda = 1.5 \mu\text{m}$. The relative fraction of light which is “tapped” off by the via can be adjusted by varying the via width, or by fabricating the via in a manner that provides dielectric contrast relative to the core material.

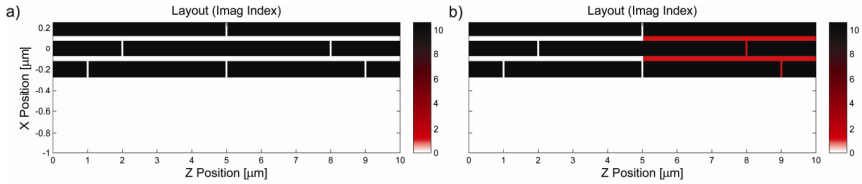


Fig. 9. Schematic cross sectional view of a simulated multilayer plasmonic interferometer. (a) Control device, in which the waveguide core is everywhere non-absorbing. (b) The waveguide core is given non-zero absorption at positions $z > 5\mu\text{m}$, simulating photoinduced absorption of the signal beam by means of a pump beam (not shown in the schematic).

From simulation performed on two stacked metal/dielectric/metal waveguides linked by a single slit as the optical via, we find that the via acts as a junction for modes incident from the waveguide, with $\sim 18\%$ of the power being reflected back in the waveguide, $\sim 46\%$ transmitted along the waveguide, and $\sim 36\%$ tapped by the via in the bottom waveguide. On the other hand, when the SPP is incident from the via side, the junction acts as a 50/50 splitter with negligible back-reflection.

We additionally consider filling the waveguide cores with a medium with non-zero absorption, $n = 2.02 + i\kappa$ in the half-space $z > 5\ \mu\text{m}$, as in Fig. 9(b). This investigation is inspired by the experimental results previously presented, and the values of imaginary index κ used here are chosen in order to achieve attenuation per unit length comparable to the experiment. However, in the current simulation we make two key simplifying assumptions. First, we do not explicitly simulate the propagation of a “pump” beam which activates the optical absorption in the buried layer, and second, we assume that the real part of the index stays constant even as κ varies. The simulated performance of a multilayer plasmonic interferometer is illustrated in Colour plate 5. The left column shows the magnetic field H_y magnitude, providing a clear view of propagation and standing wave patterns within the waveguide stack. In the right column we display the real part of the E_z field under the same conditions, which illustrate more clearly the “beams” of light which emanate from the output slits. One arm of the interferometer ($z < 5\ \mu\text{m}$) is always filled with a non-absorbing medium ($n = 2.02$), while the other arm ($z > 5\ \mu\text{m}$) is filled with an absorber having the following complex index of refractions: (a) $n = 2.02 + 0.025i$, (b) $n = 2.02 + 0.1i$, (c)

$n = 2.02 + 1.0i$. The device is illuminated by a plane wave incident on the top input slit and produces three output beams through slits in the bottom metal surface. As absorption is increased, the right output beam is entirely suppressed, the center output beam is diminished, and the left output beam is unchanged.

4.2. Incoupling strategies

In order to consider integration of our plasmonic modulators or other subwavelength active devices as constituents of dense subwavelength photonic networks, we must also address strategies for efficiently coupling light in the plasmonic waveguides, and develop design strategies to achieve low overall loss. In this section, we employ FDTD simulations to survey alternative coupling schemes which are achievable with minimal incremental changes to the device structures we have already fabricated. In view of an increased compatibility with the existing Si-based microphotronics and mature CMOS technology, we investigated metal/dielectric/metal stack consisting of a core of 160-nm-thick Si layer, with 10-nm-thick silicon dioxide, which may be codoped with an active material, such as CdSe or Si QDs, showing photoinduced carrier absorption for the signal SPP. As cladding layer we consider 400-nm-thick Ag films on both sides of the thin waveguide. In all simulations the incident light is TM polarized, monochromatic, continuous wave excitation at $\lambda = 1.55 \mu\text{m}$. In the chosen coordinate system the waveguide propagation axis is z . In all cases the input port, whether slit or waveguide end facet, is centered at the center of the simulation volume, with coordinates $(z, x) = (2, 0) \mu\text{m}$. At steady-state, the power which is considered “incoupled” in the plasmonic waveguide is that which passes through a monitor port consisting of a line segment which intersects the waveguide axis at $(z, x) = (2.5; -0.4:0.4) \mu\text{m}$.

The following incoupling geometries are considered:

(1) Slit incoupling (Colour plate 6). The source is a gaussian beam with $1.5\text{-}\mu\text{m}$ waist in the plane $x = 1 \mu\text{m}$, about a half micrometer above the surface. The slit is an air-filled opening transverse to the waveguide, 400 nm wide, 490 nm deep through the metal cladding and halfway into the Si core. Note that the assumption that the focal radius equals λ is

somewhat arbitrary but intended as a “best case” estimate. The reported incoupling coefficient represents the energy coupled into the dielectric waveguide in the $+z$ direction; due to the symmetry of this coupling scheme, of course the same amount also couples into the $-z$ direction.

(2) Metal-clad taper incoupling (Colour plate 7). The source is the lowest order TM mode of an air-clad Si-core waveguide with a 970-nm thick core, same thickness as the entire stack. This waveguide is joined to the 160-nm-thick Si core of the metal/dielectric/metal stack by a 1 μm segment of concave parabolic taper. The tapered segment is clad in Ag.

(3) Thin (160 nm) waveguide incoupling (Colour plate 8). The source is the lowest order TM mode of a 160-nm-thick Si waveguide in air.

For comparison, we also consider a tapered waveguide incoupling geometry where the source is the lowest order TM mode of an air-clad Si-core waveguide with a 970-nm-thick core, joined to the 170-nm-thick Si core of the metal/dielectric/metal stack by a 1 μm segment of concave parabolic taper, clad in air; and to conclude, end-fire incoupling by using a gaussian beam with 1.5- μm waist, incident normal to the end facet of an abruptly truncated metal/dielectric/metal waveguide. The results of the FDTD data analysis are reported in Table 1.

We find that the insertion loss for the 160-nm-waveguide end-fire scheme, Table 1, is only -4.4 dB, an improvement of about 8 dB over the slit-coupling geometry. This type of analysis allows us to trade off the demand for increased performance with the desire to minimize added design complexity. Most importantly, the substantial improvement reported here can be achieved without varying the width of the Si core in the dielectric waveguide region relative to that of the core in the metal/dielectric/metal active region.

Table 1. Power incoupled to Ag/Si/Ag plasmonic waveguide.

Incoupling Geometry	Incoupled Power (%)	Incoupled Power (dB)
Slit	5.2	-12.8
Endfire	14.8	-8.3
Air-clad taper	20.4	-6.9
Metal-clad taper	24.0	-6.2
Thin (160 nm) waveguide	35.9	-4.4

Acknowledgements

We acknowledge from the Department of Energy, Basic Energy Sciences program under grant DOE DE-FG02-07ER46405.

References

1. A.A. Sawchuck and T.C. Strand, Digital optical computing, *Proc. IEEE* **72**, 758–779 (1984).
2. A. Huang, Architectural considerations involved in the design of an optical digital-computer, *Proc. IEEE* **72**, 780–786 (1984).
3. A.V. Krishnamoorthy and D.A.B. Miller, Scaling optoelectronic-VLSI circuits into the 21st century: a technology roadmap, *IEEE J. Sel. Top. Quantum Electron.* **2**, 55–76 (1996).
4. K.-N. Chen, M.J. Kobrinsky, B.C. Barnett and R. Reif, Comparisons of Conventional, 3-D, Optical, and RF Interconnects for On-Chip Clock Distribution, *IEEE Trans. Electron Devices* **51**, 233–239 (2004).
5. ITRS, International Technology Roadmap for Semiconductors, *Emerging Research Devices* (2005).
6. S.M. Jensen, The non-linear coherent coupler, *IEEE J. Quantum Electron.* **18**, 1580–1583(1982).
7. J.L. Jewell, Y.H. Lee, M. Warren, H.M. Gibas, N. Peyghambarian, A.C. Gossard and W. Wiegmann, 3-pJ, 82-MHz optical logic gates in a room-temperature GaAs-AlGaAs multiple-quantum-well etalon, *Appl. Phys. Lett.* **46**, 918–920 (1985).
8. S.R. Friberg, Y. Silberberg, M.K. Oliver, M.J. Andrejco, M.A. Saifi, and P.W. Smith, Ultrafast all-optical switching in a dual-core fiber nonlinear coupler. *Appl. Phys. Lett.* **51**, 1135–113 (1987).
9. S.D. Smith, A.C. Walker, F.A.P. Tooley and B.S. Wherrett, The demonstration of restoring digital optical logic, *Nature* **325**, 27–31 (1987).
10. Almeida, V. R., Barrios, C. A., Panepucci, R. R. and Lipson, M. (2004). All-optical control of light on a silicon chip, *Nature*, 431, 1081–1084.
11. A.S. Liu, R. Jones, L. Liao, D. Samara-Rubio, D. Rubin, O. Cohen, R. Nicolaescu and M.A. Paniccia, High-speed silicon optical modulator based on a metal-oxide-semiconductor capacitor, *Nature* **427**, 615–618 (2004).
12. E. Kretschmann, Determination of optical constants of metals by excitation of surface plasmons, *Z. Phys.* **241**, 313–324 (1971).
13. H. Raether, *Surface plasmons on smooth and rough surfaces and on gratings* (Springer-Verlag, Tracts in Mod. Phys., Vol. 111, New York, 1988).
14. R. Zia, J.A. Schuller, A. Chandran, and M.L. Brongersma, Plasmonics: the next chip-scale technology, *Mater. Today* **9**, 20–27 (2006).
15. S.A. Maier, *Plasmonics: fundamentals and applications* (Springer, New York, 2007).

16. H.A. Atwater, The promise of plasmonics, *Sci. Am.* **296**, 56–63 (2007).
17. F.J. García-Vidal, H.J. Lezec, T.W. Ebbesen, and L. Martin-Moreno, Multiple paths to enhance optical transmission through a single subwavelength slit, *Phys. Rev. Lett.* **90**, 213901 (2003).
18. H.J. Lezec, and T. Thio, Diffracted evanescent wave model for enhanced and suppressed optical transmission through subwavelength hole arrays, *Opt. Express* **12**, 3629–3651 (2004).
19. H.F. Schouten, N. Kuzmin, G. Dubois, T.D. Visser, G. Gbur, P.F.A. Alkemade, H. Blok, G.W. 't Hooft, D. Lenstra, E.R. Eliel, Plasmon-assisted two-slit transmission: Young's experiment revisited, *Phys. Rev. Lett.* **94**, 053901 (2005).
20. P. Lalanne, J.P. Hugonin and J.C. Rodier, Theory of surface plasmon generation at nanoslit apertures, *Phys. Rev. Lett.* **95**, 263902 (2005).
21. G. Gay, O. Alloschery, B. Viaris de Lesegno, C. O'Dwyer, J. Weiner and H.J. Lezec, The optical response of nanostructured surfaces and the composite diffracted evanescent wave model, *Nature Phys.* **2**, 262–267 (2006).
22. G. Gay, O. Alloschery, B. Viaris de Lesegno, J. Weiner, and H.J. Lezec, Surface wave generation and propagation on metallic subwavelength structures measured by far-field interferometry, *Phys. Rev. Lett.* **96**, 213901 (2006).
23. O.T.A. Janssen, H.P. Urbach, and G.W. 't Hooft, On the phase of plasmons excited by slits in a metal film, *Opt. Express* **14**, 11823–11832 (2006).
24. D. Pacifici, H.J. Lezec, H.A. Atwater and J. Weiner, Quantitative determination of optical transmission through subwavelength slit arrays in Ag films: Role of surface wave interference and local coupling between adjacent slits, *Phys. Rev. B* **77**, 115411 (2008).
25. D. Pacifici, H.J. Lezec and H.A. Atwater, All-optical modulation by plasmonic excitation of CdSe quantum dots, *Nature Photon.* **1**, 402–406 (2007).
26. G. Lévêque, O.J.F. Martin, J. Weiner, Transient behavior of surface plasmon polaritons scattered at a subwavelength groove, *Phys. Rev. B* **76**, 155418 (2007).
27. J. Weiner, Phase shifts and interference in surface plasmon polariton waves, *Opt. Express* **16**, 950–956 (2008).
28. C.B. Murray, D.J. Noms, and M.G. Bawendi, Synthesis and characterization of nearly monodisperse CdE (E = S, Se, Te) semiconductor nanocrystallites, *J. Am. Chem. Soc.* **115**, 8706–8715 (1993).
29. M. Nirmal, D.J. Norris, M. Kuno, M.G. Bawendi, A.L. Efros and M. Rosen, Observation of the dark exciton in CdSe quantum dots, *Phys. Rev. Lett.* **75**, 3728–3731 (1995).
30. V.I. Klimov, A.A. Mikhailovsky, S. Xu, A. Malko, J.A. Hollingsworth, C.A. Leatherdale, H.J. Eisler and M.G. Bawendi, Optical gain and stimulated emission in nanocrystal quantum dots, *Science* **290**, 314–317 (2000).
31. C.A. Leatherdale, W.-K. Woo, F.V. Mikulec and M.G. Bawendi, On the absorption cross section of CdSe nanocrystal quantum dots, *J. Phys. Chem. B* **106**, 7619–7621 (2002).

32. A. Polman, Erbium implanted thin film photonic materials, *J. Appl. Phys.* **82**, 1–39 (1997).
33. V.I. Klimov, C.J. Schwarz, D.W. McBranch, C.A. Leatherdale and M.G. Bawendi, Ultrafast dynamics of inter- and intraband transitions in semiconductor nanocrystals: Implications for quantum-dot lasers, *Phys. Rev. B* **60**, R2177–R2180 (1999).
34. V.I. Klimov, Optical nonlinearities and ultrafast carrier dynamics in semiconductor nanocrystals, *J. Phys. Chem. B* **104**, 6112–6123 (2000).